Motion artifacts associated with *in vivo* endoscopic OCT images of the esophagus

Wei Kang,[1,†] Hui Wang,[1,†] Zhao Wang,[1] Michael W. Jenkins,[1] Gerard A. Isenberg,[2] Amitabh Chak,[2] and Andrew M. Rollins[1,2,*]

[1]*Department of Biomedical Engineering, Case Western Reserve University, 10900 Euclid Avenue, Cleveland, Ohio 44106, USA*

[2]*Department of Medicine, Case Western Reserve University, 10900 Euclid Avenue, Cleveland, Ohio 44106, USA*

[†]*These authors contributed equally to this work*

[*]*rollins@case.edu*

Abstract: 3-D optical coherence tomography (OCT) has been extensively investigated as a potential screening and/or surveillance tool for Barrett's esophagus (BE). Understanding and correcting motion artifact may improve image interpretation. In this work, the motion trace was analyzed to show the physiological origin (respiration and heart beat) of the artifacts. Results showed that increasing balloon pressure did not sufficiently suppress the physiological motion artifact. An automated registration algorithm was designed to correct such artifacts. The performance of the algorithm was evaluated in images of normal porcine esophagus and demonstrated in images of BE in human patients.

OCIS codes: (110.4500) Optical Coherence Tomography; (170.2150) Endoscopic imaging; (100.3010) Image reconstruction techniques.

References and links

1. S. Jackle, N. Gladkova, F. Feldchtein, A. Terentieva, B. Brand, G. Gelikonov, V. Gelikonov, A. Sergeev, A. Fritscher-Ravens, J. Freund, U. Seitz, S. Schröder, and N. Soehendra, "In vivo endoscopic optical coherence tomography of esophagitis, Barrett's esophagus, and adenocarcinoma of the esophagus," Endoscopy **32**(10), 750–755 (2000).
2. G. Zuccaro, N. Gladkova, J. Vargo, F. Feldchtein, E. Zagaynova, D. Conwell, G. Falk, J. Goldblum, J. Dumot, J. Ponsky, G. Gelikonov, B. Davros, E. Donchenko, and J. Richter, "Optical coherence tomography of the esophagus and proximal stomach in health and disease," Am. J. Gastroenterol. **96**(9), 2633–2639 (2001).
3. J. M. Poneros, S. Brand, B. E. Bouma, G. J. Tearney, C. C. Compton, and N. S. Nishioka, "Diagnosis of specialized intestinal metaplasia by optical coherence tomography," Gastroenterology **120**(1), 7–12 (2001).
4. G. Isenberg, M. V. Sivak, Jr., A. Chak, R. C. Wong, J. E. Willis, B. Wolf, D. Y. Rowland, A. Das, and A. Rollins, "Accuracy of endoscopic optical coherence tomography in the detection of dysplasia in Barrett's esophagus: a prospective, double-blinded study," Gastrointest. Endosc. **62**(6), 825–831 (2005).
5. X. Qi, M. V. Sivak, G. Isenberg, J. E. Willis, and A. M. Rollins, "Computer-aided diagnosis of dysplasia in Barrett's esophagus using endoscopic optical coherence tomography," J. Biomed. Opt. **11**(4), 044010 (2006).
6. J. A. Evans, J. M. Poneros, B. E. Bouma, J. Bressner, E. F. Halpern, M. Shishkov, G. Y. Lauwers, M. Mino-Kenudson, N. S. Nishioka, and G. J. Tearney, "Optical coherence tomography to identify intramucosal carcinoma and high-grade dysplasia in Barrett's esophagus," Clin. Gastroenterol. Hepatol. **4**(1), 38–43 (2006).
7. J. A. Evans, B. E. Bouma, J. Bressner, M. Shishkov, G. Y. Lauwers, M. Mino-Kenudson, N. S. Nishioka, and G. J. Tearney, "Identifying intestinal metaplasia at the squamocolumnar junction by using optical coherence tomography," Gastrointest. Endosc. **65**(1), 50–56 (2007).
8. M. J. Cobb, J. H. Hwang, M. P. Upton, Y. Chen, B. K. Oelschlager, D. E. Wood, M. B. Kimmey, and X. Li, "Imaging of subsquamous Barrett's epithelium with ultrahigh-resolution optical coherence tomography: a histologic correlation study," Gastrointest. Endosc. **71**(2), 223–230 (2010).
9. S. H. Yun, G. J. Tearney, B. J. Vakoc, M. Shishkov, W. Y. Oh, A. E. Desjardins, M. J. Suter, R. C. Chan, J. A. Evans, I. K. Jang, N. S. Nishioka, J. F. de Boer, and B. E. Bouma, "Comprehensive volumetric optical microscopy in vivo," Nat. Med. **12**(12), 1429–1433 (2007).
10. B. J. Vakoc, M. Shishko, S. H. Yun, W. Y. Oh, M. J. Suter, A. E. Desjardins, J. A. Evans, N. S. Nishioka, G. J. Tearney, and B. E. Bouma, "Comprehensive esophageal microscopy by using optical frequency-domain imaging (with video)," Gastrointest. Endosc. **65**(6), 898–905 (2007).

#146201 - $15.00 USD Received 19 Apr 2011; revised 1 Aug 2011; accepted 7 Aug 2011; published 4 Oct 2011

11. M. J. Suter, B. J. Vakoc, P. S. Yachimski, M. Shishkov, G. Y. Lauwers, M. Mino-Kenudson, B. E. Bouma, N. S. Nishioka, and G. J. Tearney, "Comprehensive microscopy of the esophagus in human patients with optical frequency domain imaging," Gastrointest. Endosc. **68**(4), 745–753 (2008).
12. H. L. Fu, Y. Leng, M. J. Cobb, K. Hsu, J. H. Hwang, and X. Li, "Flexible miniature compound lens design for high-resolution optical coherence tomography balloon imaging catheter," J. Biomed. Opt. **13**(6), 060502 (2008).
13. J. Xi, L. Huo, Y. Wu, M. J. Cobb, J. H. Hwang, and X. Li, "High-resolution OCT balloon imaging catheter with astigmatism correction," Opt. Lett. **34**(13), 1943–1945 (2009).
14. D. C. Adler, C. Zhou, T. H. Tsai, H. C. Lee, L. Becker, J. M. Schmitt, Q. Huang, J. G. Fujimoto, and H. Mashimo, "Three-dimensional optical coherence tomography of Barrett's esophagus and buried glands beneath neosquamous epithelium following radiofrequency ablation," Endoscopy **41**(09), 773–776 (2009).
15. M. J. Suter, P. A. Jillella, B. J. Vakoc, E. F. Halpern, M. Mino-Kenudson, G. Y. Lauwers, B. E. Bouma, N. S. Nishioka, and G. J. Tearney, "Image-guided biopsy in the esophagus through comprehensive optical frequency domain imaging and laser marking: a study in living swine," Gastrointest. Endosc. **71**(2), 346–353 (2010).
16. W. Kang, H. Wang, Y. Pan, M. W. Jenkins, G. A. Isenberg, A. Chak, M. Atkinson, D. Agrawal, Z. Hu, and A. M. Rollins, "Endoscopically guided spectral-domain OCT with double-balloon catheters," Opt. Express **18**(16), 17364–17372 (2010).
17. G. W. Falk, T. W. Rice, J. R. Goldblum, and J. E. Richter, "Jumbo biopsy forceps protocol still misses unsuspected cancer in Barrett's esophagus with high-grade dysplasia," Gastrointest. Endosc. **49**(2), 170–176 (1999).
18. J. A. Jankowski, R. F. Harrison, I. Perry, F. Balkwill, and C. Tselepis, "Barrett's metaplasia," Lancet **356**(9247), 2079–2085 (2000).
19. M. J. Suter, K. A. Gallagher, M. S. Shishkov, G. Y. Lauwers, J. R. Thiesse-Namati, B. E. Bouma, N. S. Nishioka, and G. J. Tearney, "Monitoring the esophageal response to radio frequency ablation with optical frequency domain imaging," presented at SPIE Photonics West, San Francisco, CA, 7893–3 Jan. 2011.
20. C. Zhou, T.-H. Tsai, H.-C. Lee, D. C. Adler, J. M. Schmitt, Q. Huang, J. G. Fujimoto, and H. Mashimo, "Endoscopic 3D-OCT for in-vivo assessment of endoscopic treatments of Barrett's esophagus and esophageal cancer," presented at SPIE Photonics West, San Francisco, CA, 7893–4 Jan. 2011.
21. J. Y. Ha, M. Shishkov, M. Colice, W. Y. Oh, H. Yoo, L. Liu, G. J. Tearney, and B. E. Bouma, "Compensation of motion artifacts in catheter-based optical frequency domain imaging," Opt. Express **18**(11), 11418–11427 (2010).
22. Y. Chen, A. D. Aguirre, P. L. Hsiung, S. Desai, P. R. Herz, M. Pedrosa, Q. Huang, M. Figueiredo, S. W. Huang, A. Koski, J. M. Schmitt, J. G. Fujimoto, and H. Mashimo, "Ultrahigh resolution optical coherence tomography of Barrett's esophagus: preliminary descriptive clinical study correlating images with histology," Endoscopy **39**(7), 599–605 (2007).
23. M. Rosales, P. Radeva, O. Rodriguez-Leor, and D. Gil, "Modelling of image-catheter motion for 3-D IVUS," Med. Image Anal. **13**(1), 91–104 (2009).
24. M. G. Danilouchkine, F. Mastik, and A. F. van der Steen, "Accuracy in prediction of catheter rotation in IVUS with feature-based optical flow--a phantom study," IEEE Trans. Inf. Technol. Biomed. **12**(3), 356–365 (2008).
25. K. Y. Leung, R. A. Baldewsing, F. Mastik, J. A. Schaar, A. Gisolf, and A. F. van der Steen, "Motion compensation for intravascular ultrasound palpography," IEEE Trans. Ultrason. Ferroelectr. Freq. Control **53**(7), 1269–1280 (2006).
26. C. Gatta, O. Pujol, O. Rodriguez Leor, J. Mauri Ferre, and P. Radeva, "Fast rigid registration of vascular structures in IVUS sequences," IEEE Trans. Inf. Technol. Biomed. **13**(6), 1006–1011 (2009).
27. G. van Soest, J. G. Bosch, and A. F. van der Steen, "Azimuthal registration of image sequences affected by nonuniform rotation distortion," IEEE Trans. Inf. Technol. Biomed. **12**(3), 348–355 (2008).
28. A. A. Amini, T. E. Weymouth, and R. C. Jain, "Using Dynamic-Programming for Solving Variational-Problems in Vision," IEEE Trans. Pattern Anal. Mach. Intell. **12**(9), 855–867 (1990).
29. D. Geiger, A. Gupta, L. A. Costa, and J. Vlontzos, "Dynamic programming for detecting, tracking, and matching deformable contours," IEEE Trans. Pattern Anal. Mach. Intell. **17**(3), 294–302 (1995).
30. I. Matthews, T. Ishikawa, and S. Baker, "The template update problem," IEEE Trans. Pattern Anal. Mach. Intell. **26**(6), 810–815 (2004).
31. K. Hinkelmann and O. Kempthorne, *Design and analysis of experiments*, 2nd ed., (Wiley-Interscience, Hoboken, NJ, 2008).
32. G. A. Maccioli, D. R. Kuni, G. Silvay, J. M. Evans, J. M. Calkins, and J. A. Kaplan, "Response of lower esophageal contractility to changing concentrations of halothane or isoflurane: a multicenter study," J. Clin. Monit. **4**(4), 247–255 (1988).
33. C. Mather, S. Raftery, and C. Prys-Roberts, "Somatic movement and oesophageal motility during isoflurane anaesthesia," Br. J. Anaesth. **69**(1), 40–44 (1992).
34. J. W. Dundee, N. J. Halliday, K. W. Harper, and R. N. Brogden, "Midazolam. A review of its pharmacological properties and therapeutic use," Drugs **28**(6), 519–543 (1984).
35. M. B. Wallace, "Somewhere over the rainbow," Gastrointest. Endosc. **71**(2), 354–356 (2010).
36. S. H. Yun, G. J. Tearney, J. F. de Boer, and B. E. Bouma, "Motion artifacts in optical coherence tomography with frequency-domain ranging," Opt. Express **12**(13), 2977–2998 (2004).

#146201 - $15.00 USD Received 19 Apr 2011; revised 1 Aug 2011; accepted 7 Aug 2011; published 4 Oct 2011

37. X. Qi, Y. Pan, M. V. Sivak, J. E. Willis, G. Isenberg, and A. M. Rollins, "Image analysis for classification of dysplasia in Barrett's esophagus using endoscopic optical coherence tomography," Biomed. Opt. Express **1**(3), 825–847 (2010).
38. J. P. Thirion, "Image matching as a diffusion process: an analogy with Maxwell's demons," Med. Image Anal. **2**(3), 243–260 (1998).
39. D. Rueckert, L. I. Sonoda, C. Hayes, D. L. Hill, M. O. Leach, and D. J. Hawkes, "Nonrigid registration using free-form deformations: application to breast MR images," IEEE Trans. Med. Imaging **18**(8), 712–721 (1999).

1. Introduction

2-D cross-sectional endoscopic optical coherence tomography (EOCT) is capable of differentiating gastrointestinal (GI) mucosal types and detecting dysplasia in Barrett's esophagus (BE) [1–8]. Recently, improvements in the technology have enabled endoscopic 3-D volumetric imaging (2 to 5cm in length) of BE [9–16]. The new technology allows for interrogation of a 20 cm^2 mucosal area or more, and therefore avoids the sampling error inherent in standard clinical biopsy-based surveillance examinations [17-18]. If the volumetric image sets are precisely reconstructed, 3-D visualization and analysis may allow one to detect dysplasia in BE with less error than standard tissue biopsy alone. EOCT is also capable of visualizing Barrett's glands [8, 19-20]. The number of Barrett's glands in post-radio-frequency-ablated esophagus has been proposed as a metric to evaluate the eradication rate of radio-frequency ablation (RFA) for BE treatment. However, when the same glands appearing in subsequent cross-sectional images are misaligned due to motion, quantification is difficult. Registration of glands is necessary to avoid miscounting.

Volumetric esophageal imaging has been accomplished by use of medical balloons mounted on catheter-based imaging probes to center the probe in the lumen. The balloon serves to stabilize the side-viewing probe and suppress motion artifacts while the probe is rotated rapidly and pulled back slowly, scanning the OCT beam on the esophageal lumen while recording a helical 3-D image set (Fig. 1(a)). However, even with the balloon, significant image distortion due to motion artifacts has been commonly observed [9–13,15-16,21]. Figure 1(b) schematically illustrates the three components of motion artifact present in helical esophageal scanning. The beam rotates one revolution with slight pullback to the position indicated by the dashed beam to generate one image. In the time between two successive images, the tissue experiences a relative displacement due to motion, which causes image distortion, or motion artifact. The radial component of the motion artifact (in the direction of the probe beam) and the rotational component (in the direction of the probe rotation) create distortion detectable within individual frames and between successive frames. The longitudinal component of the artifact (in the direction of the pullback) is not clearly differentiated without detecting additional information, such as a two-dimensional Doppler shift (e.g. Ref [21].). In this work, motion artifacts refer to the radial and rotational components if not otherwise specified. Figure 1(c) illustrates an example of radial motion artifact by displaying a stack of cross-sectional OCT images obtained from a swine esophagus *in vivo* without pullback of the probe. The third axis is time (i.e. successive frames) and the time-radial plane illustrates how the reconstruction is substantially distorted radially due to motion of the tissue. Figure 1(d) is an *en face* plane extracted from the same volume within the layer of the muscularis mucosa (approximately 300 μm from the mucosal surface). In this view, rotational distortion is clearly observed. Therefore, in order to faithfully represent the imaged tissue, an image registration algorithm is needed for 3-D reconstruction of the EOCT images [9–11,16]. Such an algorithm will also facilitate the quantification of the size and number of the subsquamous Barrett's glands (approximately 100 μm in diameter) [8,14,22]. In addition to accurate reconstruction, a registration algorithm will allow the analysis of tissue motion. By tracing the motion, the analysis may reveal the limitations of balloon-based probe technology for motion suppression. It may also guide further optimization of balloon design parameters such as diameter and pressure [15,16].

#146201 - $15.00 USD Received 19 Apr 2011; revised 1 Aug 2011; accepted 7 Aug 2011; published 4 Oct 2011

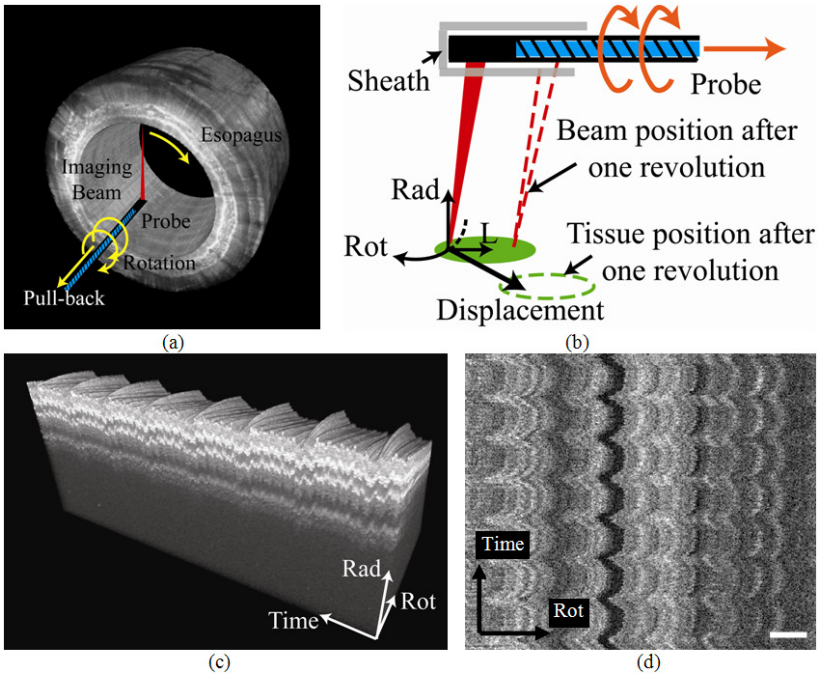

Fig. 1. (a) The helical imaging scheme of the side-view probe. (b) The motion artifacts are caused by the relative motion between the tissue and the sheath during image acquisition. (Rad: radial; Rot: rotational; L: longitudinal) (c) The radial-time plane of a 3-D reconstruction shows the radial displacement. (d) The *en face* visualization of the plane 300 μm deep in (c) shows rotational motion. (Bar: 1mm)

Post-acquisition registration technologies have been developed for correcting motion artifact in esophageal OCT images with limited success. The lumen surface has been aligned to a cylinder to compensate for radial distortion [9–11,16], but this did not compensate for rotational artifact. This alignment also requires lumen segmentation, which is time-consuming if not implemented automatically. A Doppler interferometer combined with the OCT system estimated the radial and longitudinal motion artifact in a rotating phantom [21]. It was not readily practical for *in vivo* imaging because a second optical fiber limited the probe rotation. The registration algorithms utilized for removing motion artifact in intravascular ultrasound (IVUS) [23–26] and intravascular OCT imaging [27] may provide insights into effective algorithms for esophageal OCT. Researchers have registered both surface contours [23] and tissue structures [26] to correct for motion. Esophageal OCT images consist of similar contours and image structures. However, a global, rigid translational and/or rotational transformation did not effectively suppress the common non-uniform rotational distortion (NURD) [27]. Applying registration algorithms to smaller regions of interest (ROI) could improve the results by enabling deformable transformations. Using smaller ROIs for both IVUS and intravascular OCT, researchers have assumed highly correlated speckle patterns between successive frames [24,27]. However, speckle patterns between successive esophageal OCT images are not correlated because the lumen is relatively large and displacement between successive frames is significant. A practical approach for esophageal OCT imaging may compare the structural similarity between ROIs of moderate sizes, e.g. the local block matching (LBM) algorithm [25], and then apply local transformations to correct for rotational motion. The ROI size should be optimized so that it is large enough to contain structural features for correlation, but also small enough to correct for NURD.

The primary goal of this work was to develop a fully automated registration algorithm to correct motion artifacts, especially rotational artifact. First, the algorithm estimated the

#146201 - $15.00 USD Received 19 Apr 2011; revised 1 Aug 2011; accepted 7 Aug 2011; published 4 Oct 2011

mucosal surface by detecting the strong radial gradient. After the images were radially aligned, LBM detected the rotational artifact. Different size ROIs were compared. Esophageal OCT images acquired from swine *in vivo* were reconstructed for evaluation. Images from patients with high-grade dysplastic BE were also acquired to demonstrate the registration of Barrett's glands. The secondary goal of this work was to analyze the tissue motion trace and determine the origins and evaluate suppression of motion by the balloon. The results showed that increasing balloon pressure did not completely suppress the physiological motion artifact.

2. Methods

2.1 Spectral-domain endoscopic OCT System

The spectral-domain EOCT (SD-EOCT) system utilized in this study has been described in Ref [16], and a schematic is shown in Fig. 2(a). The rotary-joint-pullback unit generated the helical scanning pattern enabling volumetric imaging. The side-viewing catheter probe rotated at 10 revolutions per second. The balloon was attached to center and stabilized the probe. An air regulator (700-BC; Controlair Inc., Amherst, NH) controlled the air flow from an aquarium pump (Rena Air 400; Aquarium Pharmaceuticals, Inc., Chalfont, PA) to maintain the pressure inside the balloon (0 to 140 mmHg). The diameter of the balloon was 18 mm at 30 mmHg and 25 mm at 130 mmHg in the open air. The spectrometer acquired 40,000 A-scans per second. Each cross-sectional image contained 4,000 A-scans. The A-scan range of the system is 4.2 mm in air. The axial and transversal resolutions of the system were 13 µm and 33 µm respectively, in air. The longitudinal pitch of cross-sectional images was 33 µm.

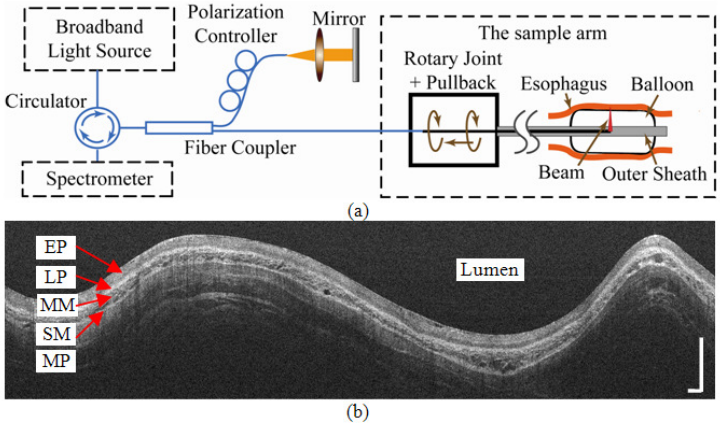

Fig. 2. (a) System schematic of the SD-EOCT system. The rotary-joint-pullback unit generated the helical scanning pattern. The balloon was attached to center and stabilize the probe. (b) A representative rectangular view before the polar coordinate transformation. EP: epithelium; LP: lamina propria; MM: muscularis mucosa; SM: submucosa; MP: muscularis propria. Bars: 1mm.

A representative rectangular view before transformation into a circular, anatomic view is shown in Fig. 2(b). Each vertical line is one A-scan, and the image is simply constructed by arranging all A-scans horizontally. The vertical and horizontal directions in the rectangular view are radial and rotational in the esophagus, respectively. The upper surface is the air-balloon-tissue interface, which is about 9 mm away from the probe.

Inconsistencies in probe rotation speed cause mechanical motion artifact and have been previously reported [10]. The inconsistency was compensated by recording the orientation (angle) of the A-scans. The A-scans were triggered at a constant frequency and later interpolated to generate A-scans evenly spaced rotationally. In our system, A-scan data were acquired at a constant angular increment. 4,000 triggers per revolution were provided by the

#146201 - $15.00 USD Received 19 Apr 2011; revised 1 Aug 2011; accepted 7 Aug 2011; published 4 Oct 2011

servomotor drive (S200; Kollmorgen, Radford, VA) in the rotary-joint-pullback unit to the line scan camera (SU-LDH 1024; SUI Goodrich Princeton, NJ) in the spectrometer.

2.2 Image acquisition in a swine model

Three swine (20-40 kg) were imaged under a protocol as previously reported [16]. The swine were sedated with Telazol (10 mg/kg), intubated, ventilated (13 breaths/min) and maintained under anesthesia with Isoflurane (1.5~2%) for the duration of the procedure. Heart rate (80 to103 beats/min) was monitored.

An initial endoscopic inspection of the esophagus was performed with the OCT catheter hidden in the accessory channel of the endoscope. The endoscope was inserted approximately 45 cm from the mouth. The balloon was then projected out of the accessory channel, inflated and maintained at a constant pressure of 30 mmHg. First, a cross-section at one longitudinal position was imaged repeatedly without pulling the probe. Images were acquired for 25 seconds with ventilation (2-D sequences *in vivo*). The ventilation was then paused for 25 seconds to obtain images without motion artifact caused by respiration. After resuming the ventilation, 3-D volumetric images were obtained by pulling the probe for 1 cm (3-D sequences *in vivo*). The probe was then pushed forward 1 cm to the initial position. The process was repeated for 50, 70, 90, 110 and 130 mmHg. Three swine were imaged in total following this protocol. A cross section of one excised swine esophagus was also imaged repeatedly (2-D sequences *ex vivo*) without pulling the probe to provide a control without physiological motion artifact.

2.3 Image acquisition in patients for BE surveillance

The clinical pilot study was conducted in University Hospitals Case Medical Center (UHCMC), Cleveland, Ohio, under a protocol approved by the Institutional Review Board of UHCMC. Patients undergoing endoscopic surveillance for BE were eligible for inclusion in the study. Patients with a diagnosis of adenocarcinoma or esophageal stricture were excluded. Informed consent was obtained from each patient.

An initial endoscopic inspection was performed before acquiring OCT images. When a segment of BE (> 2 cm in length) was identified, the balloon was inserted through the accessory channel. The balloon was deployed and inflated within the BE segment under endoscopic guidance. 3-D volumetric images were obtained by pulling the probe for 1 cm. The balloon pressure is maintained at 100 mmHg. The OCT catheter was extracted after OCT imaging. Biopsies were obtained from 4 quadrants of the imaged segment for histopathology. The surveillance procedure then continued according to the standard protocol [17].

2.4 Image registration to suppress motion artifacts

Registration was performed on the rectangular views (e.g. Fig. 2(b)). First, the balloon surface was automatically detected so that the images would be aligned radially. The radial gradient of each pixel was defined as as intensity difference along the A-scan. The difference was calculated by subtracting the mean intensity 30 μm above the pixel from that below the pixel. 30 μm was chosen because it was the approximate mean thickness of the balloon. The detection of the balloon surface was then formulated as a global optimization problem, which sought a contiguous curve with only one pixel from each A-scan. The summation of the radial gradient value on the curve was a global maximum among all the possible curves. The optimization was achieved by dynamic programming [28,29]. A one-dimensional low-pass filter was also applied to smooth the curve. To correct for radial motion, the detected interface was aligned to a straight line by translating each A-scan in the radial direction.

LBM was applied to estimate the rotational motion. LBM matched ROIs in each image to the previous image by cross-correlation. In this work, each image was divided radially into N ROIs with an equal number of A-scans. N was varied from 1 to 20 for comparison. The structural similarity between the current ROI and its reference was defined by the cross-

#146201 - $15.00 USD Received 19 Apr 2011; revised 1 Aug 2011; accepted 7 Aug 2011; published 4 Oct 2011

correlation coefficient. The coefficient was calculated by shifting the current ROI in the rotational direction with respect to its reference. The shift that yielded the maximal coefficient was considered to be the rotational displacement of the middle A-scan in the ROI. After motion estimation by LBM, the displacements of all the A-scans between two middle A-scans were linearly interpolated. As a result, A-scans were assigned new unevenly-spaced rotational coordinates. The registered image was then reconstructed by bilinear interpolation at even rotational spacing. LBM does not distinguish tissue motion from actual variation in the longitudinal anatomical structure of the tissue, such as blood vessel branches. This phenomenon has been commonly studied in computer vision [30]. LBM simply translates the current ROI rotationally so that it appears as similar to the reference ROI as possible. This might generate small errors compared to the actual anatomy, which would accumulate as LBM is applied hundreds of times, and distort the longitudinal anatomical structure. We implemented a simple solution based on the assumption that anatomical changes occur more slowly than physiological motion. We applied a spatial filter to the motion trace to remove the slowly varying apparent rotational components. The filter was a 5th order Butterworth high pass filter with the cutoff frequency at the ventilation rate (13 breaths/min = 0.022 frame^{-1}).

The registration algorithm was implemented using MATLAB (MathWorks, Natrick, MA) software. Parallel computing technology and an 8 core computer with 3 GB memory were utilized to run the algorithm.

2.5 Evaluation of surface detection and overall registration

The surface segmentation algorithm was evaluated with 3-D sequences *in vivo*. 2 images were selected from each pressure level in each swine. The lumen dimensions in these 36 images differed significantly, enabling the robustness of the segmentation to be examined. A blinded reader (Z. W.) manually segmented the contour of the tissue surface. The manually segmented contour was considered the gold standard. The segmentation error was defined as the distance between the manually segmented pixel and the automatically segmented pixel in the same A-scan. The mean and standard deviation of the errors of all A-scans in 36 images were calculated as evaluation metrics.

The overall alignment was evaluated on the 2-D sequences *in vivo*. Images to be evaluated were down-sampled 4 times so that random speckle did not affect the structural comparison. Images were then stacked along the time axis as shown in Fig. 1(c). The mean normalized standard deviation (MNSD) evaluated how the pixels varied along the time axis. The MNSD was defined as Eq. (1) [27]:

$$\langle \sigma \rangle = \frac{1}{N_{tis}} \sum_{(r,c)\in tissue} \frac{\sigma(p_{rc})}{\langle p_{rc} \rangle}, \tag{1}$$

where p_{rc} is the pixel intensity at row r and column c. $\langle p_{rc} \rangle$ and $\sigma(p_{rc})$ indicate the mean and the standard deviation at the position (r, c) along the sequence. In order to avoid introducing variability from background noise, MNSD was only calculated for pixels containing image signal in all images in the stack. N_{tis} was the number of pixels included in the calculation. Higher MSND indicated less similarity along the time axis, and therefore more motion artifact. MNSD was calculated in the original and corrected sequences for comparison.

2.6 Tissue motion analysis

The motion magnitude was quantified at each balloon pressure level and correlated with physiological movement. In the 2-D sequences *in vivo*, the first image in each sequence was considered to have no distortion. The middle A-scans of the N ROIs were backtracked to find their original positions. The motion trajectories of these A-scans were generated. The trajectories were then decomposed into the radial and rotational components and analyzed by Fourier transform. Fourier transform of the trajectories enabled one to identify the respiration

#146201 - $15.00 USD Received 19 Apr 2011; revised 1 Aug 2011; accepted 7 Aug 2011; published 4 Oct 2011

rate and heart rate (and their harmonics). The components of the motion trajectories corresponding to heart beat and respiratory motion were extracted from the frequency spectrum and inverse Fourier transformed The magnitude of each component was defined as the peak-to-peak amplitude divided by 2. One-way analysis of variance (ANOVA) [31] was applied to determine whether the mean magnitudes of each component were significantly different among the six pressure levels.

3. Results

3.1 Evaluation of surface detection and overall registration

The average time to process one cross-sectional image was 15 seconds. For evaluation of the mucosal surface detection, the automatically detected boundaries in images from the 3-D sequence *in vivo* were compared to expert human segmentation. The measured mean and standard deviation of the segmentation error were −0.2 and 2.8 pixels, respectively (i.e. −1.8 and 25 μm in air or −1.3 and 19 μm in tissue).

For evaluation of overall motion artifact correction, MNSD was calculated in both the original and registered 2-D sequences *in vivo*. In the LBM process, images were divided into *N* (1 to 20) ROIs for comparison and the resulting MNSDs are plotted in Fig. 3. The original sequences (*N* = 0 in Fig. 3) have much higher MNSDs than the registered sequences. When *N* = 1, the registration was similar to the global rigid transformation in Ref [26]. and resulted in a reduction of MNSD of 21% on average. As *N* increased, the images in each sequence became more and more similar, so that for N = 20, the MNSD was reduced by 26% on average. This improvement is attributed mainly to the correction for NURD. However, the

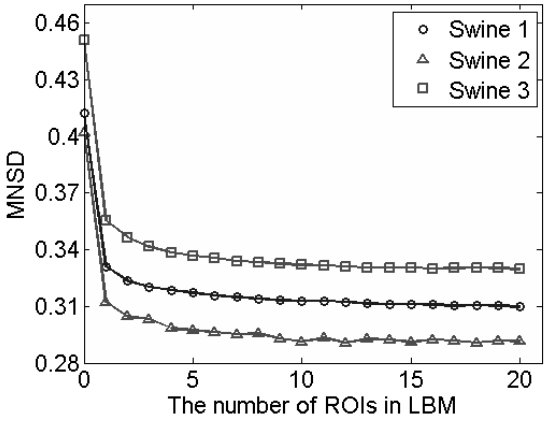

Fig. 3. Evaluation of automatic registration using 2-D sequences recorded in 3 swine. The mean normalized standard deviation (MNSD) quantified how the pixels varied between subsequent frames in the sequence. MNSD of the registered sequences was calculated as a function of the number of ROIs used for LBM. The MNSD scale begins at 0.28, which was the reference baseline MNSD attributable to image noise only, with no sample motion.

improvement reached 25% at N = 10, and only trivial additional improvement was measured with more ROIs. It is noted that the MNSDs of the three original sequences are different, but the improvements in MNSDs of the registered sequences are similar (around 0.09). The MNSD was also measured in a 2-D sequence *ex vivo* in order to exclude motion artifact. The measured MNSD *ex vivo* was 0.28, meaning that the residual error in the corrected *in vivo* sequences is attributable to noise in the images and residual longitudinal motion artifacts (see section 3.2). The registrations demonstrated in Fig. 4 were computed with *N* = 10.

#146201 - $15.00 USD Received 19 Apr 2011; revised 1 Aug 2011; accepted 7 Aug 2011; published 4 Oct 2011

3.2 Demonstration of registration

The registration results are demonstrated in Fig. 4 using 2-D and 3-D sequences. Figure 4(a) shows an *en face* view of the muscularis mucosa taken from a 2-D sequence from the excised esophagus. Without constant angular triggering the magnitude of mechanical (not physiological) rotational artifact was as high as 300 μm. With constant angular triggering, only slight residual mechanical motion artifact is present. Note that the distortion along the time axis is subtle compared to Fig. 4(b), from an *in vivo* 2-D sequence where physiological motion artifact is prominent. Residual mechanical motion was not a significant cause of distortion. Figure 4(c) displays the motion-corrected *en face* view of Fig. 4(b). The rotational distortion is significantly suppressed, although the image pattern along the time axis shows variability compared to Fig. 4(a). This residual variability along the time axis was probably caused predominantly by longitudinal tissue movement. For illustration purposes, a straight line was selected in the corrected image (red line shown in Fig. 4(c)) and the position of the A-scans on that line is shown in the unprocessed image (red line shown in Fig. 4(b)). Figures 4(d) and 4(e) represent typical unprocessed and corrected, respectively, radial-longitudinal cross-sections from a 3-D sequence *in vivo*. Their corresponding *en-face* views within the muscularis mucosa layer (after radial correction in both cases) are displayed in Figs. 4(f) and (g), where the yellow arrows indicate the rotational positions of Figs. 4(d) and 4(e), respectively. The radial position of Fig. 4(g) is indicated by the yellow arrow in Fig. 4 (e). The saw-tooth patterns in both the radial and rotational directions were corrected and the tissue layers were aligned. The muscularis mucosa has a rich vascular network, which can be visualized more clearly in the corrected *en face* view. Figures 4(h) and 4(i) are enlarged views of the regions indicated in the dashed yellow rectangles in Figs. 4(f) and 4(g), respectively. The registration algorithm was able to recover detailed features in Fig. 4(i) which were otherwise obscure in Fig. 4(g).

Figure 5(a) shows a cross-sectional image from a patient enrolled in our clinical study. Histopathology showed that the patient had high-grade dysplasia in the esophageal segment imaged with OCT. The mucosal layers are obscured in the OCT image, which is consistent with previous observations of dysplastic tissue [4,5]. Dark oval glandular structures can be clearly observed (example indicated by number 1). The size, shape and position within the mucosa resemble Barrett's glands [8,14]. The esophagus was larger than the balloon in this case and therefore not fully expanded, leaving a gap between the tissue surface and the balloon. Figures 5(b) and 5(c) are *en face* views at 300 μm deep within the dysplastic esophagus before and after rotational motion artifact correction. The numbers 1, 2 and 3 indicate representative regions in the images where motion artifact resulted in misalignment and distortion of the glandular structures. Regions 1 in Figs. 5(b) and 5(c) correspond to region 1 in Fig. 5(a). The shape and number of glands are significantly distorted in the *en face* view before correction. The registration algorithm clearly restored the accurate glandular morphology in Fig. 5(c) by re-aligning the glands along subsequent cross-sectional images. This will reduce ambiguity when interpreting the shape and number of glands in those regions.

3.3 Tissue motion analysis

The radial and rotational motions measured from a representative 2-D image sequence (first 100 images) in swine 2 at a balloon pressure of 90 mmHg are plotted in Fig. 6(a). The motion

#146201 - $15.00 USD Received 19 Apr 2011; revised 1 Aug 2011; accepted 7 Aug 2011; published 4 Oct 2011

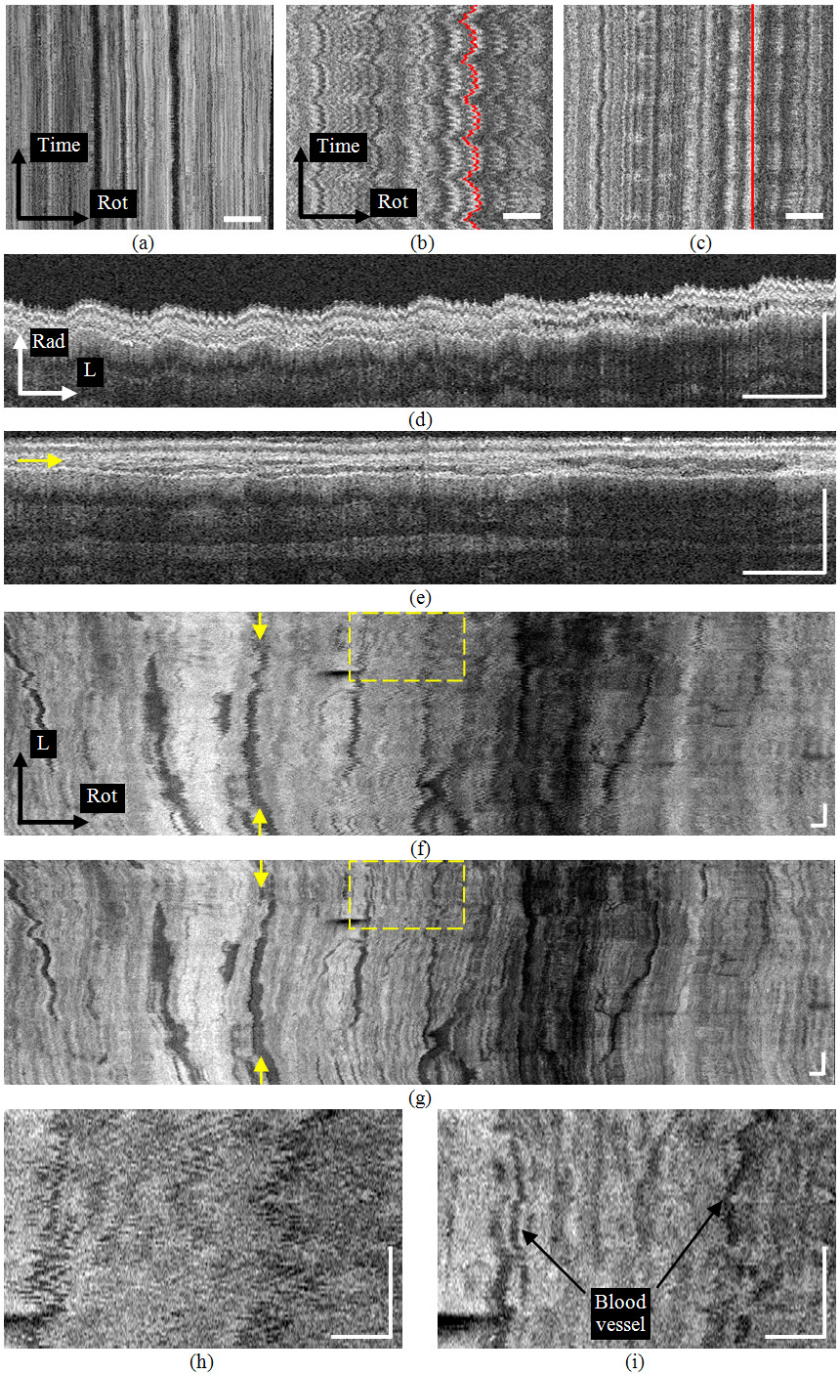

Fig. 4. (a) The *en face* view of the muscularis mucosa layer in the excised esophagus from a 2-D time sequence of images. (b) The *en face* view of the *in vivo* 2-D sequence where physiological motion artifact is prominent. (c) The registered *en face* view of (b). (d) A radial-longitudinal view from the original 3-D sequence *in vivo*. (e) The registered view of (d). The arrow indicates the position of (g). (f) The *en face* view from the original 3-D sequence. Arrows indicate the position of (d). (g) The registered view of (f). Arrows indicate the position of (e). (h) The enlarged view of the square in (f). (i) The enlarged view of the square in (g). (Rad: radial; L:longitudinal; Rot:rotational. Bars: 1mm)

#146201 - $15.00 USD Received 19 Apr 2011; revised 1 Aug 2011; accepted 7 Aug 2011; published 4 Oct 2011

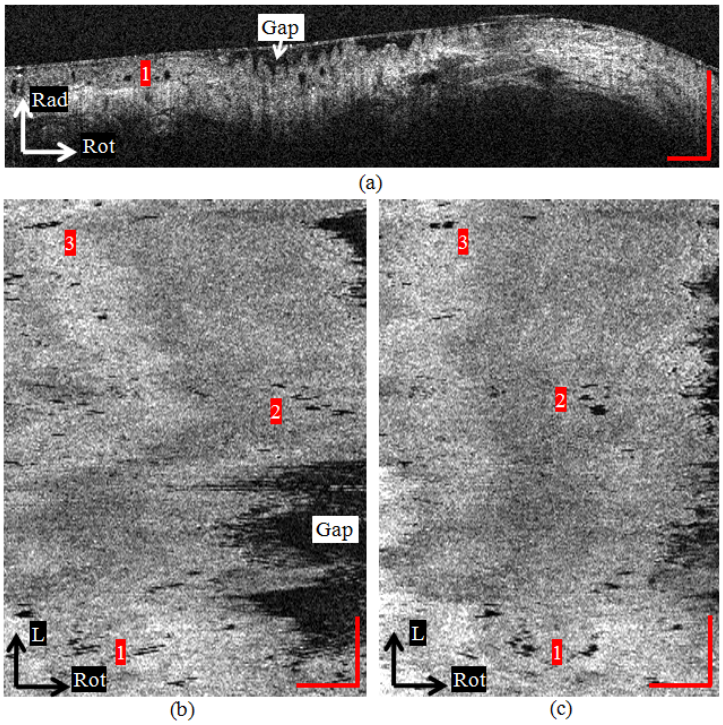

Fig. 5. (a) A cross-sectional image of BE with high-grade dysplasia. Dark oval glandular structures can be clearly observed (example indicated by number 1). (b) The *en face* view at 300 μm deep within the dysplastic esophagus before rotational motion artifact correction. The shape and number of glands are significantly distorted. (c) The *en face* view after rotational correction. The registration algorithm more clearly reveals the glandular morphology

traces were zero padded and Fourier transformed. The amplitude spectra are plotted in Fig. 6(b). The peaks at 0.22 Hz and 1.32 Hz correlate well with the respiration rate (0.22 Hz) and heart rate (1.36 Hz) measured independently. The 0.22 Hz peaks and their harmonics (at 0.46 Hz and 0.68 Hz) disappeared when the ventilation paused, confirming that they are caused by respiration. It is evident that the physiological movement in the living animal is the main origin of motion artifacts in balloon-stabilized EOCT esophageal images. The mean and standard deviation of both physiological motions (respiration and heart beat) in both the radial and rotational directions, at six levels of balloon pressure are plotted in Fig. 6(c). One-way ANOVA showed there were no significant differences among the mean magnitudes at the six pressure levels ($p>0.05$) with the exception of the rotational component of respiration. In the latter case, the mean magnitudes remained above 0.2 mm. Pair-wise analysis of the rotational component of respiration showed that the means at 30 and 50 mmHg were significantly lower than the means at 90, 110 and 130 mmHg. The magnitude plot in Fig. 6(c) shows that neither respiratory nor cardiac related motion artifacts were suppressed by increasing the balloon diameter/pressure.

4. Discussion

The mechanical motion artifact was a significant source of image distortion if not suppressed. It was observed in our system that motion magnitude was on the order of hundreds of microns at a frequency higher than the heart rate. This probably originated from the eccentric manufacturing and/or assembly of the rotary joint, catheter probe and outer sheath. The suppression method in this work assumed that the rotation was transmitted through a

#146201 - $15.00 USD Received 19 Apr 2011; revised 1 Aug 2011; accepted 7 Aug 2011; published 4 Oct 2011

rotationally rigid body because the torque was transferred through a flexible shaft designed for this purpose. This assumption was verified experimentally (data not shown). The motion

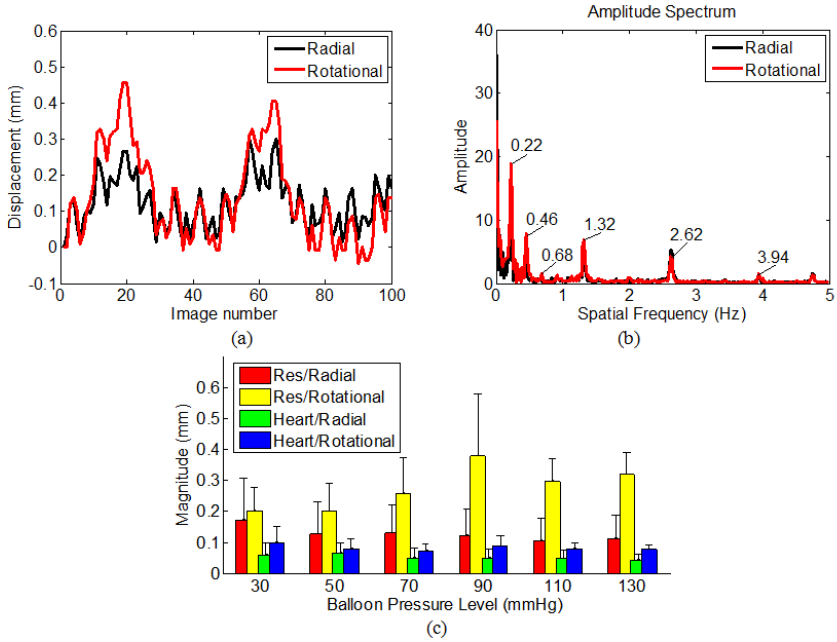

Fig. 6. (a) The radial and rotational motions measured from a representative 2-D image sequence (first 100 images). (b) The amplitude spectra of (a). (c) The mean and standard deviation of both physiological motions (respiration and heart beat) in both the radial and rotational directions, at six levels of balloon pressure.

nonlinearity at both the distal and proximal ends of the probe was highly similar. By triggering the data acquisition at constant angular increments in the rotary joint, the mechanical motion artifact at the probe was effectively suppressed. The cause of the residual mechanical artifact is not fully understood. One possibility is that the motion at the distal and proximal ends was not completely identical, so that the proximal nonlinearity did not perfectly represent the distal nonlinearity.

The esophagus in the swine model was imaged with ventilation control and heart rate monitoring. This setting allowed for the identification of physiological origins of motion artifacts. A limitation of the swine model was that peristalsis had not been observed in either endoscopy or OCT. The suppression of peristalsis was likely caused by the Isoflurane [32,33]. General anesthesia of the animal was necessary to avoid the otherwise intense body movement. However, mild anesthetics, such as Midazolam, are used for endoscopy in human patients rather than general anesthesia [34]. Therefore, peristalsis can be observed by endoscopy in patients undergoing BE surveillance. Patient's hiccups, coughs or other random body movements due to mild sedation, as well as peristalsis, are likely to make the motion artifacts more complicated [35].

This study analyzed and corrected image misalignment due to motion in EOCT. It should also be noted that motion also causes Doppler-induced depth error, reduction in spatial resolution, and signal-to-noise ratio degradation [36]. Analysis and correction of these effects requires assessment of the tissue velocity of each A-scan. Velocity assessment is beyond the capability of the proposed registration algorithm here because it only estimated the relative displacement between frames.

The potential clinical utility of the registration algorithm was demonstrated in 3-D images of BE. The algorithm was able to correct the distorted glandular structure which was caused

#146201 - $15.00 USD Received 19 Apr 2011; revised 1 Aug 2011; accepted 7 Aug 2011; published 4 Oct 2011

by motion. The algorithm relieves the burden of manual alignment and resolves the ambiguity when multiple glands are present within a small region. This may enable more accurate estimation of the quantity when counting the glands. In the future, a computer segmentation algorithm may further be developed to automatically count the number and analyze the shape of glands. Such an algorithm is highly desired when there are hundreds, if not thousands, of BE images from one single patient.

The automated registration algorithm was efficient for suppressing in-plane motion artifacts. Dynamic programming reliably detected the balloon surface because the contrast between the lumen and the balloon was consistently higher than other layered structures in the image. We note that the balloon and tissue were not in full contact in Fig. 5. The algorithm detected and aligned the balloon surface, rather than the tissue surface. Using the balloon as a reference, the surface topology of BE tissue was preserved, which may be useful as a diagnostic feature of dysplasia [37]. However, this reconstruction was based on the observation that the gap between the balloon and tissue surface changed slowly as the probe was pulled. If the motion between balloon and tissue is significant and the gap changes rapidly, then aligning the balloon surface will not completely remove the relative motion artifact from the tissue. LBM assumed uniform rotational motion within each individual ROI (N = 10). The assumption was valid, because the time to obtain such an ROI (10 msec for N = 10) was much less than the period of the heart beating (~0.6 second) or respiration (~5 second). LBM in this work was a simplified deformable registration technique which only estimated the rotational deformation (or NURD). In the radial direction, rigid translation was sufficient to register lines and correct motion, as expected because all pixels in an A-line are collected in parallel in 25 μsec. More sophisticated deformable registration technologies may be applied at the cost of intensive computation load [38,39]. However, because the noise inherent in the images contributes to approximately two third of the total MNSD of the unregistered sequence, new registration technologies may only provide marginal additional improvement.

A practical pressure range of 30 to 130 mmHg was selected to investigate the effect of balloon pressure on suppression of physiological motion artifact. These limits were selected because the esophagus was not fully expanded when the pressure was lower than 30 mmHg, while the esophageal diameter varied little at pressures higher than 90 mmHg. It was noted that the inflated diameter of the balloon in the esophagus was smaller than that in the open air because of esophageal tension. Even with balloon technology, the magnitude of the physiological motion artifacts (hundreds of microns) was comparable to the epithelial thickness (about 200 microns on average in our case) or the dimension of glandular structure [8,14,22]. The radial-longitudinal and *en-face* views were so severely distorted that little information about the tissue could be extracted without correction. The physiological origin of motion artifact has been previously observed [9], and larger balloons were proposed to suppress motion [15]. However, this study showed that higher balloon pressure/larger balloons did not suppress the physiological motion artifacts more than lower pressure levels. Therefore minimum pressure needed to distend the lumen and center the catheter is apparently sufficient for esophageal EOCT. Keeping the balloon at lower pressure or smaller diameter may be more preferable to avoid perforating the esophagus. Furthermore, the glandular structure and vascular pattern in the muscularis mucosa became less visible at higher pressures.

Understanding the motion artifact may facilitate the clinical application of laser marking technology [15], wherein a high-power laser beam is proposed to mark abnormal tissue identified by OCT screenings for later biopsy. The radial motion in the esophagus was on the order of the Rayleigh range of the laser beam, and the rotational motion was much larger than the spot size at the focus. These motions could be taken into account when optimizing the exposure for laser marking.

#146201 - $15.00 USD Received 19 Apr 2011; revised 1 Aug 2011; accepted 7 Aug 2011; published 4 Oct 2011

5. Conclusion

An accurate and fully automated algorithm was demonstrated to suppress the in-plane motion artifacts in OCT esophageal imaging, evaluated in an *in vivo* swine esophageal model and demonstrated in 3-D BE images. The registered volumetric images revealed the otherwise distorted microstructure in the esophageal mucosa. The motion artifacts were correlated with physiological movement (respiration and heart beat), and quantified. It was shown that physiological motion artifact was not physically suppressed by the balloon regardless of the balloon pressure.

Acknowledgements

The project described was support by National Institute of Health, Grant Number R03 EB004044-01, RO1 CA114276 and RO1 HL 083048. The content is solely the responsibility of the authors and does not necessarily represent the official views of the National Institute of Health.

#146201 - $15.00 USD Received 19 Apr 2011; revised 1 Aug 2011; accepted 7 Aug 2011; published 4 Oct 2011